The coupling of microwave radiation to surface plasmon polaritons and guided modes via dielectric gratings

A. P. Hibbins[a] and J. R. Sambles
Thin Film Photonics Group, School of Physics, University of Exeter, Exeter EX4 4QL, England

C. R. Lawrence
Defence Evaluation and Research Agency, Farnborough GU14 0LX, England

It is shown that an absorbing dielectric layer, sinusoidally modulated in height, on top of a planar metal substrate, may be used to provide coupling between both *s*- and *p*-polarized incident microwave photons and surface plasmon polaritons, which propagate along the metal–dielectric interface. The study is carried out using paraffin wax as the dielectric material on an aluminum-alloy plate and the wax is sufficiently thick such that it may also support a guided mode. Energy reradiated from these excited modes into diffracted orders is recorded by monitoring the specular beam reflectivity as a function of wavelength ($7.5 < \lambda_0 < 11.3$ mm) and azimuthal angle of incidence ($0° < \varphi < 90°$). The azimuthal-angle-dependent reflectivity scans are fitted using a multilayer, multishape differential formalism to model conical diffraction with a single set of parameters describing the grating profile, and the permittivity and thickness of the wax layer. © *2000 American Institute of Physics.* [S0021-8979(00)02606-2]

I. INTRODUCTION

It is well known that a wave, which is a solution of Maxwell's equations, may exist at a surface bounding two homogeneous media of different dielectric constants. When one medium is a dielectric and the other is a metal, this mode is known as the surface plasmon polariton (SPP). The mode is nonradiative if the surface is planar, and is characterized by a phase velocity greater than that of the light in the adjacent dielectric.[1] In order to excite this mode resonantly, the in-plane momentum of the incident radiation must be suitably enhanced. One way of achieving this is to use a coupling prism in the Otto[2] or Kretschmann–Raether[3] geometry. A diffraction grating may also be used to couple incident radiation into the surface mode where the corrugated interface provides the necessary in-plane wave-vector enhancement in integer multiples of the grating wave vector $\mathbf{k_g}$ ($k_g = 2\pi/\lambda_g$, where λ_g is the grating pitch) such that the surface plasmon wave vector $\mathbf{k_{SPP}}$ satisfies

$$\mathbf{k_{SPP}} = n_d \mathbf{k}_0 \sin\theta \pm N\mathbf{k}_g. \tag{1}$$

Here N is an integer, $n_d = \epsilon_d^{1/2}$ is the refractive index of the dielectric, $\lambda_0 = 2\pi/k_0$ is the wavelength of the incident radiation, and θ is the polar angle of incidence. If the azimuthal angle φ, defined as the angle between the plane of incidence and the grating wave vector, is equal to zero then all the diffracted beams lie in the plane of incidence and Eq. (1) reduces to a scalar equation.

The "classical" grating coupling geometry uses a single corrugated metal–dielectric interface, and when grating coupled in this way, the SPP propagates along this *corrugated* boundary. Since the periodic surface may diffract energy associated with the mode into diffracted orders, the propagation length of the mode is reduced. Other workers have shown that the radiative damping of the mode is proportional to the square of the grating amplitude.[1,4,5]

In this study an alternative grating geometry is used, where the metallic surface along which the SPP propagates is planar. Deposited on top of the metallic substrate is a corrugated dielectric overlayer of mean thickness t. In this work, the dielectric overlayer is petroleum wax, the refractive index of which at the microwave wavelengths studied here is ~1.5, similar to that of glass at visible wavelengths. The upper, semi-infinite dielectric is air. It is the corrugated air–dielectric boundary that excites diffracted orders and provides the required enhanced momentum to couple radiation to the SPP (TM_0 mode) associated with the wax–metal interface. This geometry is similar in some respects to the Otto arrangement that uses a high-index prism to create an evanescent field across an air gap and couple the field to a SPP on the planar metal–air interface. Here, the prism is simply substituted for a corrugated overlayer. This coupling geometry for the excitation of surface plasmons appears to have been first used by Müller *et al.*[6] They successfully coupled 632.8 nm radiation to the SPP mode, although their study was restricted to the classical mount ($\varphi = 0°$). Their sample consisted of an evaporated silver planar substrate, on top of which was a 5 nm layer of gold and a photoresist layer containing an interferographically produced grating. In addition, if the dielectric overlayer is sufficiently thick, it will also be able to support TE and higher order TM "leaky" guided modes. Dakss *et al.*[7] demonstrated how corrugated layers can be used as a mechanism to excite guided modes in thin films, and this technique has more recently been used in the conical mount ($\varphi \neq 0°$) by Veith *et al.*[8]

In contrast to the optical wavelengths where Joule heat-

---

[a]Author to whom correspondence should be addressed; electronic mail: A.P.Hibbins@Exeter.ac.uk

ing damps the SPP, metals at microwave frequencies behave as near-perfect conductors. Hence a SPP that travels along a planar boundary between semi-infinite air and a metal substrate will have an almost infinite propagation distance. However in the geometry presented here, there are two independent damping processes that may act on the SPP as it propagates along the boundary. First, the mechanism that allows radiation to couple into the SPP (i.e., the grating) will also allow the mode to radiatively decay. In a previous study that illustrates the resonant excitation of SPPs on a near-perfectly conducting metallic grating,[9] this damping process was exploited; the width of the resonances would otherwise have been prohibitively narrow to experimentally observe. Second, although the top and bottom semi-infinite media (air and metal, respectively) are effectively nonabsorbing at these frequencies, this may not be true for the wax. Since the evanescent fields associated with the SPP mode penetrate the wax, any loss mechanisms within this overlayer ($\epsilon_{i,\text{wax}}$) will contribute a term to the damping of the mode. Both of these damping terms will contribute to the width of the surface plasmon resonance and will also have a similar effect on any guided modes propagating in the system

However, it should be appreciated that reradiation of energy from the mode back into the specular beam does not necessarily give an observable resonance loss. If the grating grooves are neither parallel nor perpendicular to the plane of incidence ($\varphi \neq 0°, 90°$), then the polarization of the reradiated signal will be different from that of the incident beam and a polarization conversion signal may be detected. In this situation, a dip in the specular R_{pp} and R_{ss} reflectivities would be observed around the resonance condition, together with an associated peak in the R_{ps} and R_{sp} responses (if $\varphi \neq 0°, 90°$). Here the subscripts refer to the incident and detected polarizations, respectively. This will occur even in the absence of absorption in the wax or reradiation of the SPP into other diffracted orders.

In this article, the reflectivity of microwave radiation from the sample is recorded as a function of wavelength λ_0 and azimuthal angle of incidence φ. It is illustrated that a dielectric grating may be used to couple both s- and p-polarized microwave radiation to a SPP that propagates along a planar, near-perfect conductor, as well as guided modes supported by the wax. The azimuthal angle φ dependent reflectivity scans are fitted to a rigorous grating modeling theory[10] using the corrugation amplitude, wax thickness, and $\epsilon_{i,\text{wax}}$ as fitting parameters.

II. EXPERIMENT

By utilizing a grating modeling theory,[10] it is possible to design a sample whose grating pitch and amplitude, and wax thickness will allow surface mode resonances to be easily identified and experimentally observed in the available wavelength range ($7.5 < \lambda_0 < 11.3$ mm). The system chosen for this study has a purely sinusoidal top interface profile $A(x) = a \cos 2\pi x/\lambda_g$ (Fig. 1), where $t \approx 2.6$ mm, $a \approx 1.5$ mm, and $\lambda_g = 15$ mm. Information is deduced about the dielectric characteristics of the wax by recording the wavelength-dependent reflectivity from a planar slab of known thickness.
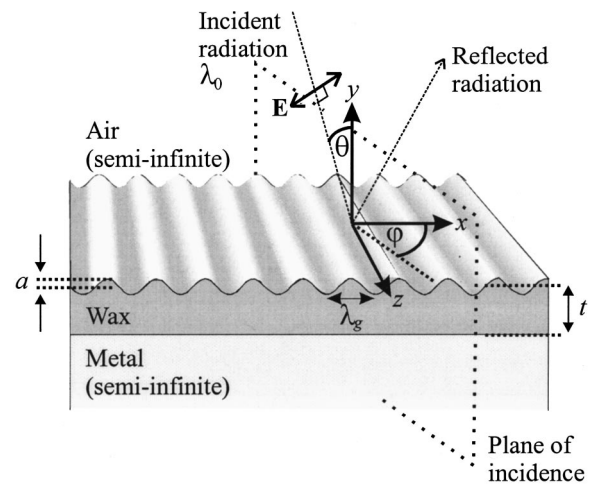

FIG. 1. Schematic diagram illustrating the sample, coordinate system, and experimental geometry used in this study. The direction of the electric field vector **E** is illustrated for the situation when p-polarized (transverse magnetic, TM) radiation is incident. Here t is the average thickness of the wax overlayer, λ_0 is the wavelength of the incident radiation, λ_g is the grating pitch, and a is the grating amplitude.

The spacing of the oscillations in the reflected signal, which are due to the interference between the radiation reflected from the top and bottom surfaces of the sample, allows the real part of the permittivity to be determined. It was calculated to be $\epsilon_{r,\text{wax}} = n_{\text{wax}}^2 = 2.29$ over the frequency range studied in this work. However the imaginary (damping) term is difficult to determine accurately by this method and is used as a fitting parameter in the subsequent theoretical modeling. In addition, the permittivity of the aluminum alloy substrate is also assumed constant[9] ($\epsilon_{\text{metal}} = -10^6 + 10^9 i$).

The sample is prepared by filling a metallic, square tray whose side is approximately 400 mm and depth 5 mm with hot wax and allowing it to cool. A metallic ''comb'' of the desired sinusoidal interface profile is manufactured using a computer-aided design and manufacture technique. It is used to remove unwanted wax from the sample by carefully dragging it across the surface until the required grating profile is obtained.

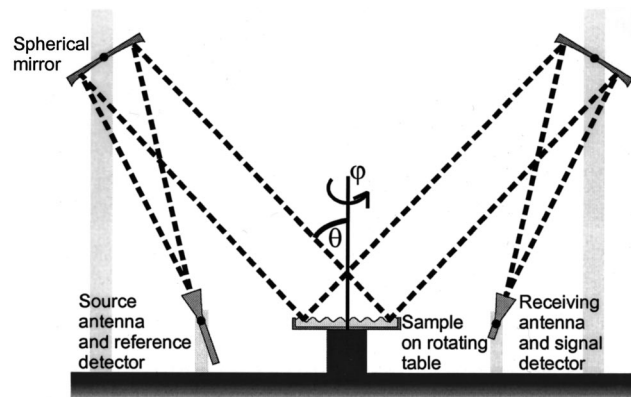Figure 2 illustrates the experimental arrangement used to

FIG. 2. Schematic diagram illustrating the apparatus used to measure the wavelength- and azimuthal-angle-dependent φ response from the sample studied in this work.
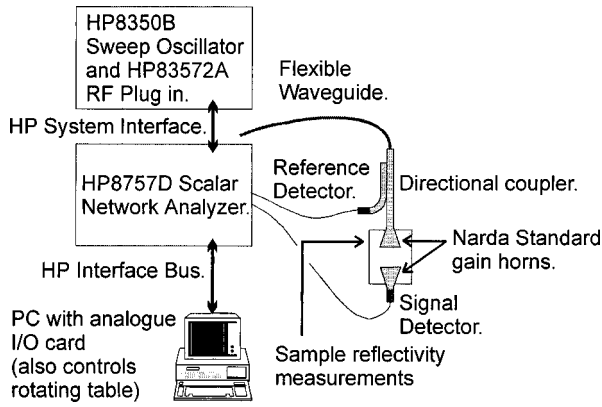
FIG. 3. Schematic representation of the interconnecting components used to record reflectivities in the 7.5–11.3 mm wavelength range.

FIG. 4. Normalized (a) R_{pp}, (b) R_{ps}, and (c) R_{ss} response of the sample as a function of frequency between 26.5 and 40 GHz (11.3 and 7.5 mm), and azimuthal angle of incidence φ. Data have been recorded between $\varphi=0°$ and $\varphi=90°$, and reflected about the x and y axis to produce full 360° polar maps.

record the reflectivity from the sample, and Fig. 3 shows a schematic representation of the interconnecting components of the system. The arrangement shown in Fig. 2 has been developed in order to reduce the undesirable effects of spherical wave fronts that may provide excitation of the SPP even without the grating. The problem of near-spherical wave fronts arises from the standard gain horn geometry and the large radiation wavelength. Typically, the beam divergence is some 20°. By placing the transmitting horn at the focus of a 2 m focal length mirror, the incident beam is well collimated. A second mirror is positioned to collect the specularly reflected beam from the grating and focused into the detector. The aluminum alloy mirrors have been milled with a diameter of 450 mm and a radius of curvature $R = 4$ m.

Variation of the magnitude of the incident wave vector in the plane of the grating may be achieved by scanning either wavelength λ_0, or angle of incidence θ or φ. Keeping the polar angle of incidence θ constant, in contrast to the conventional method of polar angle scans that are often used for experiments at visible and infrared wavelengths,[11] avoids the difficulty of scanning the detector and focusing mirror. In addition, by keeping the system fixed and only rotating the sample, the possibility of experimental errors arising from detector function is eliminated.[12]

The reflectivity data are recorded as a function of wavelength between 7.5 and 11.3 mm, and over the azimuthal angle φ range from 0° to 90° at a fixed polar angle of incidence $\theta \approx 47°$. The source and receiving horn antennae are set to pass either p (transverse magnetic, TM), or s (transverse electric, TE) polarizations, defined with respect to the plane of incidence. This enables the measurement of R_{pp}, R_{ps}, R_{ss}, and R_{sp} reflectivities. To account for any fluctuations in the emitted power from the source, the analyzer divides the output from the signal detector by that from the reference. The normalized reflectivities over the entire frequency range are downloaded from a scalar network analyzer to a PC and are saved to disk. The resulting wavelength- and angle-dependent reflectivities from the sample are normalized by comparison with the reflected signal from a flat metal plate.
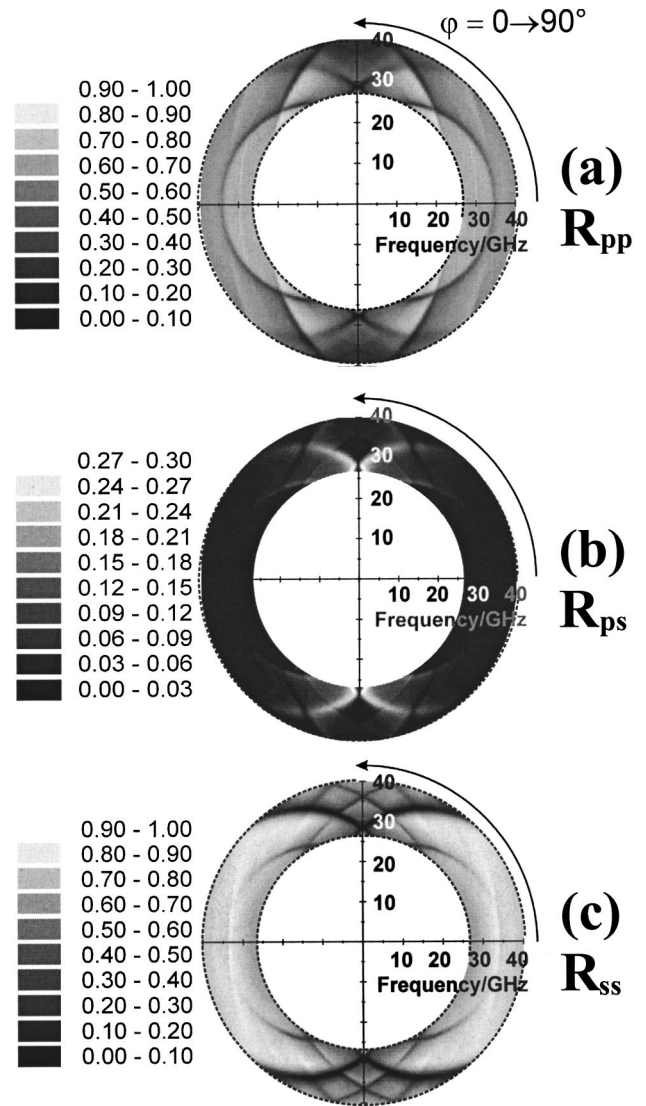
III. RESULTS

Figure 4 illustrates a polar gray-scale map of the normalized R_{pp}, R_{ps}, and R_{ss} signals from the sample as a function of frequency and azimuthal angle of incidence φ. Since the profile of the grating is nonblazed, the results from the two polarization conversion scans (R_{sp} and R_{ps}) are identical, and hence the R_{sp} response is not illustrated.

A planar air–metal interface may be represented as a single lattice point in k space, upon which a light circle of radius $n_{air}k_0$ is based. The area bounded by this circle represents the range of wave vectors that may be accessed by an incident photon from the air side. SPPs and guided modes supported by a dielectric (wax) layer deposited on top of a metal substrate, both existing at higher wave vectors than that available from an incident photon ($k_{SPP} \geq k_{GM} > n_{air}k_0$); hence it is impossible to couple directly to either mode via a planar wax–air interface. However, the periodic modulation
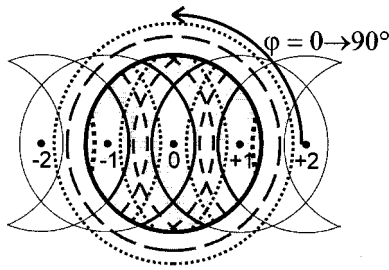
FIG. 5. A schematic reciprocal space map of the grating studied in this work with radiation of wavelength 11.0 mm incident. The numbered points are the lattice points spaced by integer multiples of the grating wave vector k_g and the solid circle centered upon the origin (of radius $n_{air}k_0$) is the incident light circle where the area it bounds (shaded) contains all the modes accessible to a real photon incident on the grating. Also centered upon the origin are dashed and dotted circles representing the momenta of the undiffracted guided mode and SPP, respectively. The periodic modulation of a diffraction grating scatters these SPP and guided-mode circles about each lattice point and the sections that fall within the incident light circle may be coupled by the incident radiation. These are represented by thick dashed and dotted lines, respectively. The diffracted light circles based upon each lattice point, and which represent the Rayleigh anomalies within the shaded area, are also shown.

of the wax overlayer diffracts the incident radiation by integer multiples of $\mathbf{k}_g$. This results in a series of diffracted light, SPP, and guided-mode circles about each reciprocal lattice point. The sections of these diffracted SPP and guided-mode circles that fall within the light circle based upon the origin may now be coupled by the incident radiation (Fig. 5). This work considers a multiwavelength study and this idea is extended by considering a series of light cones about each grating lattice point, as illustrated in Fig. 6. However for clarity, only the specular light cone is illustrated, together with cross sections through the cones for
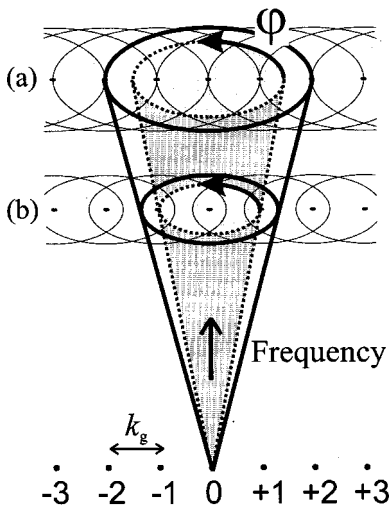

FIG. 6. Schematic diagram illustrating the reciprocal space of the experimental system studied in this work. For clarity, only the light cone that represents the momentum of the incident radiation ($n_{air}k_0$) is shown (thick lines); the cones representing the guided mode and SPP exist at a greater radius. Also shown is the light cone representing the experimental azimuthal-angle scan (dotted lines). The series of light circles labeled (a) and (b) are cross sections through the series of diffracted incident light cones with radiation of wavelength 11.3 mm (26.5 GHz) and 7.5 mm (40.0 GHz) incident, respectively. The numbered points at the bottom of the diagram illustrate the lattice points about which each light cone is centered.

frequencies 26.5 and 40.0 GHz ($\lambda_0 = 11.3$ and 7.5 mm, respectively). Incident radiation on the sample may be represented by a cone of radius $n_{air}k_0 \sin\theta$ (dashed line). By viewing from a location above the cones, one may visualize the ellipses mapped out by the intersections of this experimental angle scan with the diffracted light cones, where the points on these curves correspond to the occurrence of a Rayleigh anomaly. The Rayleigh anomaly (or pseudocritical edge) occurs when one of the diffracted orders emerges from the grating at grazing angle. This results in a sharp change in reflectivity from the grating due to the sudden redistribution of energy. These are difficult to observe in the reflectivity data due to the angle spread associated with the experiment. However the ellipses of greater radius corresponding to the coupling of radiation to SPPs and guided modes are clearly evident.

During the fitting process, it is useful to be able to differentiate SPPs from guided modes, and recognize which diffracted order provides the coupling mechanism to each mode. However, from the data illustrated in this study so far, this is not immediately obvious. One way in which each of the modes may be identified is to use a rigorous grating theory to model their dependence on the thickness of the wax layer. The theory uses a scattering matrix technique[13] based on a multilayer and multishape conical version[8] of the differential formalism of Chandezon et al.[14] It involves the transformation of the mathematics into a new, nonrectilinear coordinate system in which the boundary conditions at the corrugated interface are more readily solved, effectively flattening the surface. This requires that the field amplitudes are represented as a Fourier expansion. A Fourier series is also used to describe the surface itself

$$A(x) = a_1 \cos(k_g x) + a_2 \cos(2k_g x) + \dots$$
$$+ a_N \cos(N k_g x) + \dots, \quad (2)$$

where a_N provides the first-order diffracting mechanism to the $\pm N$ SPP.

Figure 7 illustrates, at $\lambda_0 = 11$ mm, the predicted R_{ss} reflectivities from samples with wax thicknesses: (a) $t = 2.1$ mm, (b) $t = 2.6$ mm, (c) $t = 3.1$ mm, and (d) $t = 3.6$ mm, and $a = 1.5$ mm, $\lambda_g = 15$ mm, $\epsilon_{wax} = 2.29 + 0.00i$, and $\epsilon_{metal} = -10^6 + 10^9 i$. The theoretical data are plotted in the form of a series of reciprocal space maps, where $k_x = n_{air}k_0 \sin\theta \cos\varphi$ and $k_z = n_{air}k_0 \sin\theta \sin\varphi$. The imaginary component of ϵ_{wax} has been set to zero in order to provide maximum contrast in the diagrams. (An illustration that a variation of $\epsilon_{i,wax}$ does not affect the position of the modes in k space will be provided later.)

The modes visible in Fig. 7(a) are the diffracted SPP (TM$_0$) modes which propagate along the metal–wax interface. Note that the coupling strength to the SPP decreases to zero as $\varphi = 0°$ is approached. This is because the incident TE field has no component perpendicular to the grating surface and hence cannot create the necessary surface charge. Clearly, the evanescent fields associated with the SPP will sample the wax layer and will penetrate into the air half space. Therefore, the dispersion of the SPP will be dependent on an effective refractive index (n_{wax}^{eff}) since the degree of
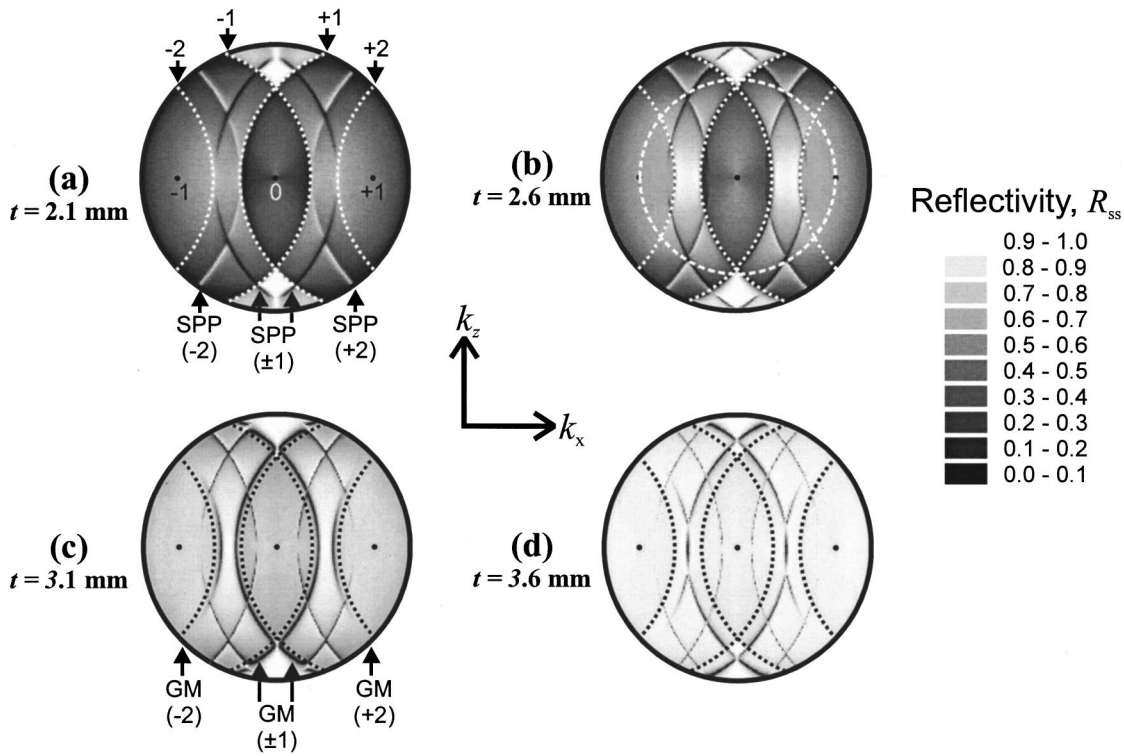
FIG. 7. Reciprocal space maps of the theoretically modeled R_{ss} signals from samples with 11 mm radiation incident and wax thicknesses (a) $t=2.1$ mm, (b) $t=2.6$ mm, (c) $t=3.1$ mm, and (d) $t=3.6$ mm (where $k_x=n_{air}k_0 \sin\theta \cos\varphi$ and $k_z=n_{air}k_0 \sin\theta \sin\varphi$). The reflectivities have only been plotted for wave vector values that are accessible to the incident photon, i.e., $(k_x^2+k_z^2)^{1/2} \leq n_{air}k_0$. The Rayleigh anomalies are labeled and highlighted with dotted lines and the SPP and guided mode (GM) are also identified and labeled with the diffracted order that provides the coupling mechanism. The equivalent experimental momentum scan undertaken at this wavelength is also shown (white, dashed circle).

penetration into the air is governed by the thickness of the wax overlayer. Hence $k_{SPP}>n(t)_{wax}^{eff}k_0$, where $n_{air} \leq n(t)_{wax}^{eff} \leq n_{wax}$ with the SPP moving to higher momentum values with increasing thickness as is clear in Fig. 7. In addition the excitation of guided modes (GMs) also becomes possible where, in contrast to the SPP, the dispersion of these modes is governed by the true refractive index of the layer n_{wax}, where $n_{air}k_0<k_{GM}<n_{wax}k_0$. The lowest order guided mode may be observed in Figs. 7(b), 7(c), and 7(d), however at $t=2.6$ mm the mode is almost coincident with the Rayleigh anomaly. In a manner similar to the SPP, the guided mode also moves away from the Rayleigh anomaly as the wax thickness is increased.

The white dashed circle superimposed on Fig. 7(b) illustrates the equivalent momentum scan undertaken in this study with radiation of wavelength $\lambda_0=11.0$ mm incident. Hence, by comparison of Fig. 7(b) with the experimental study at this fixed wavelength it is possible to identify the GM and SPP, and label the modes according to the diffracted order, which provides the coupling mechanism (Fig. 8).

Having identified the modes supported by the sample, the reflectivity data are fitted to the grating modeling theory for a series of different wavelengths. By fitting the reflectivity data to the modeling theory using a single set of parameters, it is possible to accurately parameterize the grating profile, thickness, and permittivity of the wax overlayer. Figure 9 shows a series of experimental data sets ($\square$) at wavelengths of: (a) 7.5 mm, (b) 8.5 mm, (c) 9.5 mm, and (d) 10.5 mm, showing the R_{pp}, R_{ss}, R_{ps}, and R_{ss} signals, respec-

tively. The solid curves are the theoretical fits, which are in good agreement with the experimental data. During the fitting process, the amplitude of the corrugation, thickness and real part of the permittivity of the wax, and the polar angle of incidence θ are all allowed to vary within uncertainty bounds from their measured values. The imaginary part of the permittivity of the wax is initially assumed to be zero, the pitch of the grating is $\lambda_g=15$ mm, and the permittivities of the metal and air are assumed to be $\epsilon_{metal}=-10^6+10^9 i$ and $\epsilon_{air}=1.0+0.0i$, respectively. Distortion of the grating profile
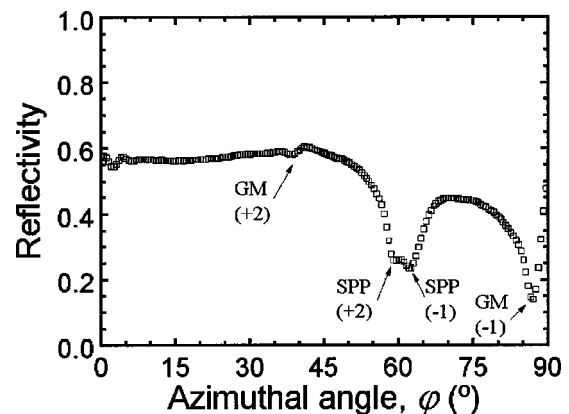

FIG. 8. The experimental R_{ss} azimuth-angle φ scan corresponding to the white, dashed line shown in Fig. 7(b) ($\lambda_0=11$ mm). The diffracted SPP and GM have been identified and labeled according to the diffracted order that provides their coupling mechanism.

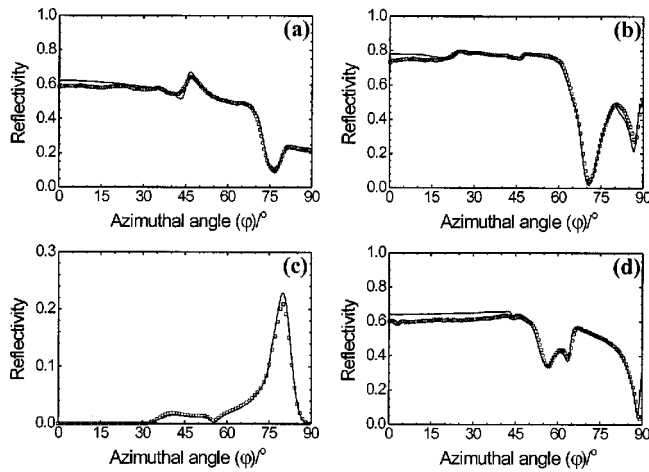FIG. 9. Typical normalized azimuthal-angle φ dependent reflectivities ($\square$) compared with the theoretically modeled results (—) created from a single set of fitting parameters. Radiation is incident on the sample at fixed polar angle of incidence of $\theta \approx 47°$ with wavelengths of: (a) $\lambda_0 = 7.5$ mm, (b) $\lambda_0 = 8.5$ mm, (c) $\lambda_0 = 9.5$ mm, and (d) $\lambda_0 = 10.5$ mm impinging on the sample. The signals recorded are: (a) R_{pp}, (b) R_{ss}, (c) R_{ps}, and (d) R_{ss}. The azimuthal-angle scans shown have been extracted from the experimental data sets illustrated in Fig. 4.

$[a_2, a_3$ in Eq. (2)] is also introduced, however it does not improve the average quality of the fits. It has previously been shown that a beam spread of approximately $\theta_{1/2} = 1°$ is required to account for finite source size and diffraction in the system,[9] therefore a small amount of beam spread is introduced into the theoretical modeling illustrated here. The grating profile, polar angle of incidence θ, and properties of the wax overlayer determined for each azimuthal scan are averaged, and the error about the mean calculated. The final fits shown are then each generated from this averaged set: $a_1 = 1.50 \pm 0.02$ mm, $t = 2.62 \pm 0.01$ mm, $\epsilon_{r,\text{wax}} = 2.29 \pm 0.01$, $\epsilon_{i,\text{wax}} = 0.04 \pm 0.01$, and $\theta = 46.8 \pm 0.1°$. To confirm the validity of the theoretical model, it is necessary to independently measure the profile of the grating. By scanning a dial gauge across the wax surface, the grating amplitude and the thickness of the wax layer are determined to be $a_1 = 1.48 \pm 0.01$ mm and $t = 2.63 \pm 0.08$ mm, respectively. Clearly, these values are within the errors of those determined via the fitting process.

IV. DISCUSSION

This work has demonstrated that it is possible to couple incident microwave radiation to the guided and SPP modes via an alternative geometry that does not require forming the grating profile directly to the metal substrate. Coupling to the SPP in this way is advantageous over the "classical" one-interface grating-coupling geometry since complicated shapes can easily be carved into a wax layer, rather than using expensive machine time to mill the shape directly into a metal. In addition, the SPP that propagates along this metal surface may only be radiatively damped since the media either side of the boundary are usually nonabsorbing. Therefore, a sufficiently large grating depth is required to shorten the lifetime of the mode and sufficiently widen the resonance so that it may be easily experimentally observed. However
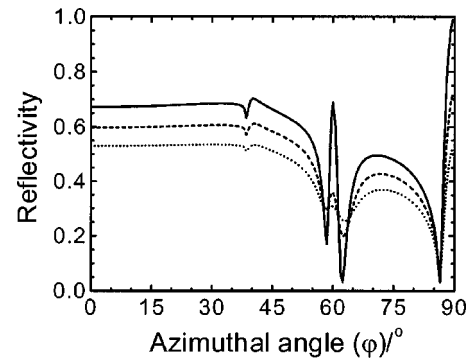

FIG. 10. Graph illustrating the effects of increasing ϵ_i of the wax layer on the R_{ss} reflected signal with radiation of wavelength $\lambda_0 = 11$ mm incident. The solid, dashed, and dotted lines correspond to $\epsilon_{i,\text{wax}} = 0.001$, $\epsilon_{i,\text{wax}} = 0.041$, and $\epsilon_{i,\text{wax}} = 0.081$, respectively. An identical set of parameters to those used to create the theoretical traces in Fig. 9 are used to produce the data shown here.

by using a corrugated dielectric overlayer with nonzero ϵ_i deposited on a planar metal surface, a second damping mechanism is introduced by which the SPP may decay. Hence the need for such large corrugation amplitudes is decreased. Figures 10 and 11 illustrate the effect of increasing the imaginary part of the permittivity of the dielectric layer on the modeled R_{ss} response and degree of absorption of the sample at $\lambda_0 = 11$ mm. They demonstrate that the positions of the modes in momentum space do not change, but the width of these resonances is increased. In addition, an absorbing overlayer will decrease the coupling strength to the SPP since the magnitude of the evanescent fields at the metal surface will be reduced. Clearly, the introduction of a non-zero ϵ_i decreases the background reflectivity level, however the degree of absorption on-resonance of a well-coupled mode is greatly enhanced. For comparison, Fig. 11 also illustrates the degree of absorption on a planar sample of the same mean thickness.

V. CONCLUSIONS

In this work, the coupling of microwave radiation via a dielectric grating to a SPP that propagates on a planar near-
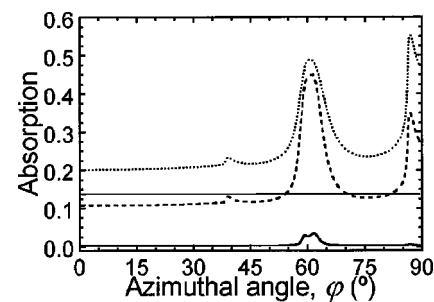

FIG. 11. Graph illustrating the effects of increasing ϵ_i of the corrugated wax layer on the absorption due to Joule heating in the sample. The sample is illuminated with incident TE radiation of wavelength 11 mm at a polar incident angle of $\theta = 47°$ with wax thickness $t = 2.6$ mm and grating amplitude $a_1 = 1.5$ mm. Illustrated are the theoretically modeled results with $\epsilon_{i,\text{wax}} = 0.00$ (thick solid line), $\epsilon_{i,\text{wax}} = 0.04$ (dashed line), and $\epsilon_{i,\text{wax}} = 0.08$ (dotted line). Also shown is the absorption due to a planar wax layer of the same mean thickness (fine solid line).

perfectly conducting metal surface has been illustrated. The dielectric material used in this study is petroleum wax and is sufficiently thick such that it is also able to support the lowest order ''guided'' mode. Due to the ease with which the required grating profile may be shaped from the wax compared to milling the profile directly into a metal substrate, this coupling mechanism may be advantageous over the ''classical'' geometry. The technique of recording the response of the sample as a function of the *azimuthal*-angle of incidence φ has been demonstrated. It is particularly useful at these wavelengths because by simply rotating the sample, it is possible to quickly gather large amounts of data by simultaneously scanning the incident wavelength. Furthermore, the incident beam has been collimated to reduce the undesirable effects of beam spread. Hence good agreement between models computed using the differential formalism of Chandezon *et al.* and the experimental reflectivities have been obtained. The fitting process has enabled the characterization of the dielectric constants of the wax, which has shown it to be slightly absorbing at these frequencies ($\epsilon_{\mathrm{wax},i} = 0.041$). In addition, the real part of the wax permittivity derived in the fitting process agrees with the value obtained via interferographic measurements. The effects of a nonzero ϵ_i in this layer is to change the coupling strengths of the diffracted SPP and guided mode resonances, and increase the range of momentum values over which energy may be coupled into the modes. The degree of absorption of the sample is also greatly enhanced on resonance of a well-coupled mode.

[1] H. Raether, *Surface Plasmons on Smooth and Rough Surfaces and on Gratings* (Springer, Berlin, 1988).
[2] A. Otto, Z. Phys. **216**, 398 (1968).
[3] E. Kretschmann and H. Raether, Z. Naturforsch. A **23a**, 2135 (1968).
[4] I. Pockrand, J. Phys. D **9**, 2423 (1976).
[5] R. C. McPhedran and M. D. Waterworth, Opt. Acta **19**, 877 (1972).
[6] K. G. Müller, M. Veith, S. Mittler-Neher, and W. Knoll, J. Appl. Phys. **82**, 4172 (1997).
[7] M. L. Dakss, L. Kuhn, P. F. Heidrich, and B. A. Scott, Appl. Phys. Lett. **16**, 535 (1970).
[8] M. Veith, K. G. Müller, S. Mittler-Neher, and W. Knoll, Appl. Phys. B: Lasers Opt. **60**, 1 (1995).
[9] A. P. Hibbins, J. R. Sambles, and C. R. Lawrence, J. Appl. Phys. **86**, 1791 (1999).
[10] T. W. Priest, N. P. K. Cotter, and J. R. Sambles, J. Opt. Soc. Am. A **12**, 1740 (1995).
[11] R. A. Watts, J. R. Sambles, and J. B. Harris, Opt. Commun. **135**, 189 (1997).
[12] A. P. Hibbins, J. R. Sambles, and C. R. Lawrence, J. Mod. Opt. **45**, 1019 (1998).
[13] N. P. K. Cotter, T. W. Priest, and J. R. Sambles, J. Opt. Soc. Am. A **12**, 1097 (1995).
[14] J. Chandezon, M. T. Dupuis, G. Cornet, and D. Maystre, J. Opt. Soc. Am. **72**, 839 (1982).